IEEE Photonics Journal
An IEEE Photonics Society Publication

Investigating Far-Field Spectra and Near-Field Features of Extraordinary Optical Transmission Through Periodic U- to H-Shaped Apertures

Volume 4, Number 2, April 2012

Hui-Hsin Hsiao
Hao-Fu Huang
Si-Chen Lee, Fellow, IEEE
Hung-Chun Chang, Senior Member, IEEE

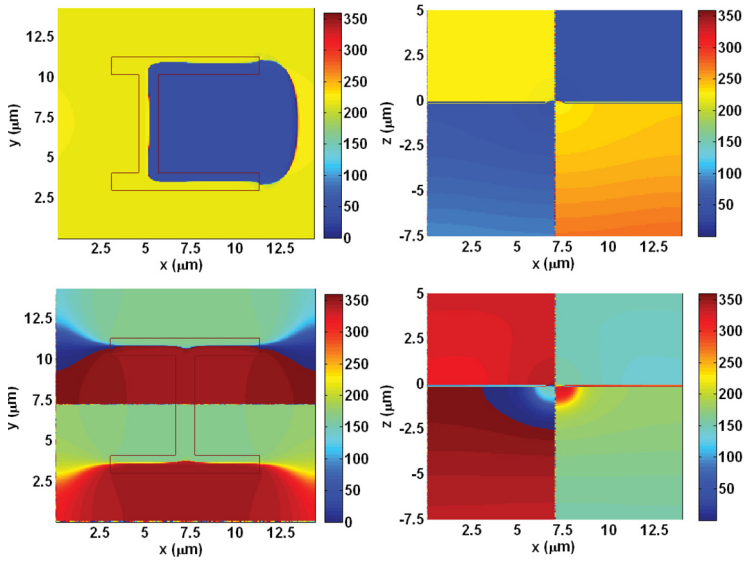

DOI: 10.1109/JPHOT.2012.2188787
1943-0655/$31.00 ©2012 IEEE

IEEE photonics SOCIETY

IEEE

Investigating Far-Field Spectra and Near-Field Features of Extraordinary Optical Transmission Through Periodic U- to H-Shaped Apertures

Hui-Hsin Hsiao,[1] Hao-Fu Huang,[2] Si-Chen Lee,[3] *Fellow, IEEE*, and Hung-Chun Chang,[4] *Senior Member, IEEE*

[1]Graduate Institute of Photonics and Optoelectronics, National Taiwan University, Taipei 10617, Taiwan
[2]Graduate Institute of Electronics Engineering, National Taiwan University, Taipei 10617, Taiwan
[3]Graduate Institute of Electronics Engineering and Department of Electrical Engineering, National Taiwan University, Taipei 10617, Taiwan
[4]Department of Electrical Engineering, Graduate Institute of Photonics and Optoelectronics, and Graduate Institute of Communication Engineering, National Taiwan University, Taipei 10617, Taiwan

DOI: 10.1109/JPHOT.2012.2188787

Manuscript received December 24, 2011; revised February 11, 2012; accepted February 15, 2012. Date of publication February 22, 2012; date of current version March 8, 2012. This work was supported in part by the National Science Council of the Republic of China under Grant NSC99-2628-M-002-008 and Grant NSC98-2221-E-002-025-MY2, in part by the Excellent Research Projects of National Taiwan University under Grant 99R80306, and in part by the Ministry of Education of the Republic of China under "The Aim of Top University Plan" Grant. Corresponding author: H.-C. Chang (e-mail: hcchang@cc.ee.ntu.edu.tw).

Abstract: By exploiting the in-house finite-difference time-domain (FDTD) program, the optical properties of a designated 2-D array of U- to H-shaped holes perforated on a metallic film are analyzed. Some specific near-field features are found to be associated with the three mechanisms underlying the transmission spectral profiles, namely, excitation of surface electromagnetic (EM) modes, Wood's anomalies (WAs), and shape resonances (SRs), thus providing a way to reveal the physical nature of the enhanced transmission phenomenon.

Index Terms: Surface plasmons, Wood's anomalies (WAs), apertures, diffraction, infrared.

1. Introduction

The phenomenon of extraordinary optical transmission (EOT) through periodically arranged subwavelength holes in metal films has attracted considerable interest over the past few decades since the pioneering work of Ebbesen *et al.* [1]. The main mechanisms responsible for this phenomenon have been widely believed to be the excitation of surface plasmon polaritons (SPPs) and Wood's anomalies (WAs) set up by periodically arranged holes [2]–[5]. In addition, several works have shown that the shape of the aperture has a strong effect on the transmission spectra [4]–[11]. For example, Koerkamp *et al.* [4] showed that shape resonances (SRs), which are in effect localized modes, play an important role in explaining the different transmission spectra between the circular and rectangular hole arrays. Ruan and Qiu [5] calculated the normalized transmission spectra and the band structure of a rectangular-shaped-hole array drilled in a perfect-electric-conductor (PEC) film to distinguish surface plasmon resonances and localized resonances. They also found that the localized modes are almost independent of the periodicity by calculating the transmission spectra of random arrays of holes. Moreover, Lee *et al.* [6] experimentally demonstrated the resonant peak dominantly depends on the hole length, which confirmed the theoretical predictions

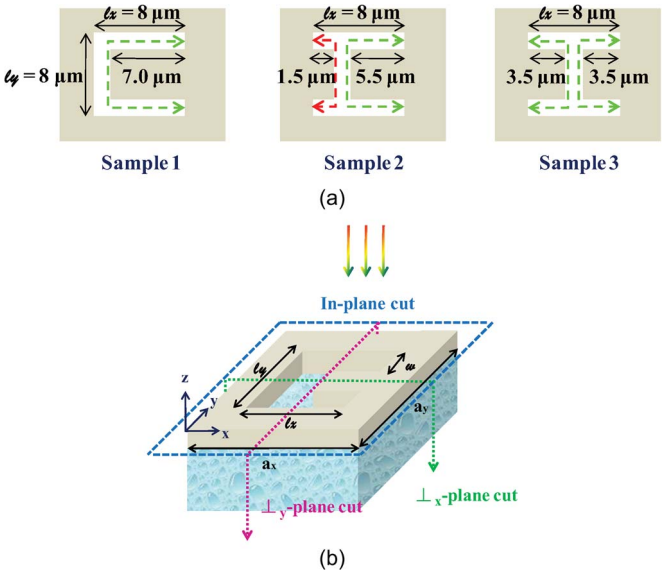

Fig. 1. (a) Top view and structural parameters of samples 1–3. (b) The unit cell and near-field plane cuts in our simulation. In-plane cut: perpendicular to the direction of propagation; perpendicular-plane cut: parallel to the direction of propagation.

of Garcia-Vidal *et al.* [8] and Ruan and Qiu [5]. Mary *et al.* [9] analyzed theoretically how SPPs and localized resonances evolve and mix when the period of the array is varied.

In order to figure out more detailed properties of extraordinary transmission, some structures with more complex-shaped apertures have been studied. For example, a range of arrays composing of double holes that slightly overlap provides an additional local field enhancement [12]–[14], which could be potentially applied to nanolithography, biochemical sensing, or nonlinear processes. Arrays with C- or U-shaped apertures [15], [16] have been designed for the purpose to redshift the shape resonant wavelength. In particular, Sun *et al.* [17] experimentally showed the transmission properties of H-shaped arrays, and Liu *et al.* [18] theoretically investigated the same structure by analyzing the transmission spectra and the near-field amplitude and phase distributions. In this paper, we study the optical properties of three similar but differently shaped apertures, which are basically composed of two horizontal slits, named *x*-arm slits, and one vertical slit, named the *y*-arm slit. The difference between them lies in the horizontal position of the *y*-arm silt, which is shifted from the alignment with the left of the two *x*-arm silts to one forth length and finally to the middle. Fig. 1(a) shows the top view and structural parameters of samples 1 (U-shaped) to 3 (H-shaped). The experimental observation of such structures has been reported [19]. The SR wavelengths could be roughly estimated by the modified cutoff wavelengths of the rectangular waveguide $\lambda_{res} = 2n_{eff}L_{res}/m$, where $n_{eff} = \sqrt{(n_{substrate}^2 + n_{air}^2)/2}$ is the effective refractive index, L_{res} is resonant length, and m is an integer [10]. However, when the shape of the aperture becomes more complex and higher order modes coexist, L_{res} would have some ambiguities to be determined. We thus use our in-house developed 3-D finite-difference time-domain (FDTD) program [20] to simulate transmission spectra and near-field distributions at several particular wavelengths to gain more understanding of the physical characteristics of the resonant modes.

Since the phasor form of electric field can be expressed as $\mathbf{E} = |E_x|e^{i\psi_x}\hat{x} + |E_y|e^{i\psi_y}\hat{y} + |E_z|e^{i\psi_z}\hat{z}$, we analyzed the distributions of electric field amplitude ($|E_x|$, $|E_y|$, and $|E_z|$) and phase (ψ_x, ψ_y, and ψ_z) simultaneously. The modulus of the electric field, $|\mathbf{E}|$, is defined by $\sqrt{|E_x|^2 + |E_y|^2 + |E_z|^2}$. We find three features are helpful in recognizing the effective SR lengths: the large magnitude of $|\mathbf{E}|$ contours clear geometry of resonant length. Within the shape resonant paths, the distribution of the

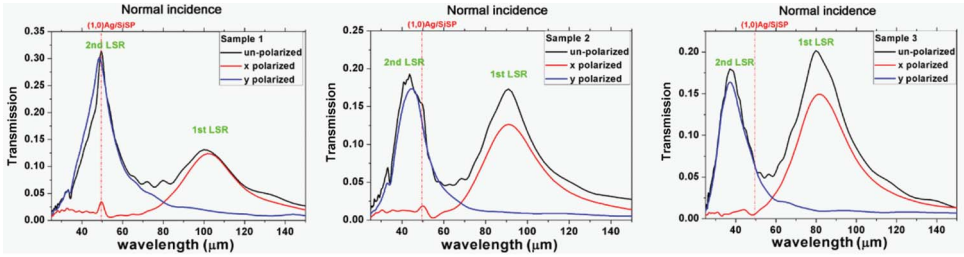

(a) (b) (c)

Fig. 2. Measured transmission spectra of (a) sample 1, (b) sample 2, and (c) sample 3. [(c) corresponds to [19, Fig. 7(a)].]

phase component parallel to the polarization of the incident light (e.g., ψ_x under *x*-polarized light) is quite homogeneous, and the phase component along the propagation direction, ψ_z, exhibits a 180° phase difference with respect to the center of the slit width. Therefore, by utilizing these thumb of rules and the symmetric requirements, we can clearly distinguish the SR lengths and also predict possible contours. For example, assigning the SR peaks of H-shaped apertures in the shorter wavelength range to be the second U-shaped resonances is not appropriate [19] since ψ_z needs to be with even symmetry with respect to the center of the *x*-coordinate under *y*-polarized light. Therefore, the resonant path will not pass the *y*-arm slit, and we find that it is indeed related to the merely two *x*-arm slits resonance. Besides, Schnell *et al.* [21], [22] recently experimentally demonstrated the antiphase of ψ_z at the metal rod center as a direct evidence of the dipolar near-field mode. This also gives us a hint for the counterpart relationship between SRs and the plasmonic resonances for metal islands.

On the other hand, many theoretical analyses of WAs and surface electromagnetic (EM) modes have revealed their origin and roles in EOT phenomenon [23]–[26], but few have shown their corresponding features in near-field analyses. For example, WA phenomenon has been known to occur when a diffracted order becomes grazing and the in-phase multiple scattering accumulates [23]. We thus find the corresponding ψ_z distribution is quite homogeneous. Besides, the weak coupling of the incident field with surface EM modes near the apertures may contribute to the transmission peaks [23], [24] and be related to the more severe phase change near the hole. Therefore, except utilizing band diagrams or the far-field spectra corresponding to different changes of the structure to distinguish different modes, we can also employ the near-field features to gain more insight of each resonance.

2. Far-Field Transmission Spectra and Dispersion Relations

Fig. 1(a) and (b) show the geometry of the subwavelength metallic structures we studied in this paper: the unit cell with lattice constants of $a_x = a_y = 14$ μm, where the length of each silt $l_x = l_y = 8$ μm, and the width of the silt $w = 1$ μm. The metal (silver) film with thickness 75 nm is coated on a silicon substrate. In addition, the relative permittivity of the silicon substrate is taken as 11.9, and that of the silver [27] is modeled by the Drude dispersion with a plasma frequency of $\omega_p = 1.3709 \times 10^{16}$ s^{-1} and a collision frequency of $\gamma = 3.2258 \times 10^{13}$ s^{-1}. These structures are illuminated by *x*-polarized and *y*-polarized plane waves, respectively, under normal incidence. The calculated transmission spectra shown in Fig. 3 are found to agree well with the measured transmission data shown in Fig. 2. Fig. 2(a)–(c) were obtained under the same experimental setup using a Bruker IFS 66 v/s Fourier-Transform Infrared (FTIR) spectrometer, as reported in [19], with Fig. 2(c) corresponding to Fig. 7(a) in [19]. In the experiment, samples 1 and 2 have the same material structures as that of sample 3, except the top view shapes differ, as shown in Fig. 1(a). The spectra exhibit very different features under *x*-polarized and *y*-polarized incident light because of the anisotropic geometry of the hole structure. The transmission minima are associated with the

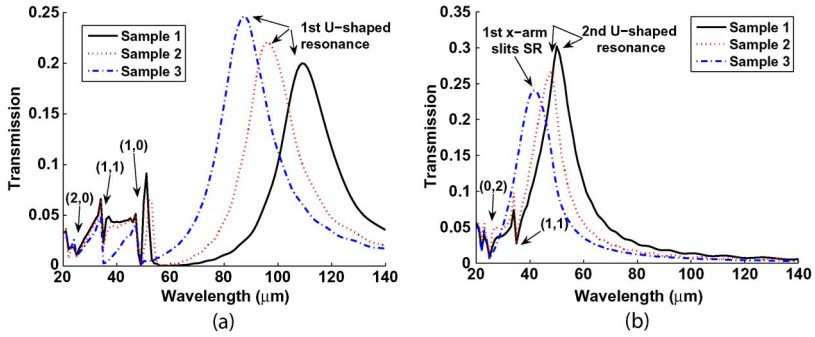

Fig. 3. Calculated transmission spectra with polarized incident light at (a) *x* polarization and (b) *y* polarization under normal incidence.

WAs which could happen when a diffracted order becomes tangent to the plane of the grating, and the free-space wavelength that satisfies WA condition under normal incidence is given by

$$\lambda_{WA} = \frac{\Lambda}{\sqrt{i^2 + j^2}} \times \sqrt{\varepsilon_d} \tag{1}$$

where i and j are integers referring to the specific orders of the WA modes in the x and y directions, respectively, $\Lambda\ (= 14\ \mu\text{m})$ is the lattice constant, and $\varepsilon_d\ (= 11.9)$ is the relative dielectric constants of silicon. Notice that only Ag/Si WAs, denoted as (i, j) mode Ag/Si WAs, will be excited in the wavelength range of 20–140 μm. Adjacent to the WA dips are some small peaks which are due to the coupling of the incident field with surface EM modes [23]–[25]. Since the property of silver is PEC-like in the far-infrared range, the surface EM modes dominantly result from the multiple scattering of the diffracted modes within the holey metal surface [24], [28]. We have examined the spectra with the silver film replaced by a perfect conductor which usually does not support surface plasmon waves. The spectra are almost the same with Fig. 3 (not shown), while the peak values corresponding to SRs increase because of the lossless material and the spectral positions of SRs are slightly blue shifted due to the lack of penetration depth for perfect conductor.

As mentioned in [19], the localized shape resonant path is mainly the U-shaped part of the hole in our case. The broadband peaks at 109 μm, 96 μm, and 87 μm for samples 1 to 3 under *x*-polarized light correspond to the 1st U-shaped resonance. The blue-shifted trend of the spectral positions from samples 1 to 3 is due to the shrinkage of the effective resonant length of aperture referring to the green path indicated in Fig. 1(a). On the other hand, the peaks at 51 μm and 47 μm in Fig. 3(b) correspond to the second U-shaped resonances for samples 1 and 2 under *y*-polarized light. The broadband resonance at 42 μm of sample 3 may seem to also be the second U-shaped resonance according to the trend. However, from the help of near-field analyses, this peak is related to the two *x*-arm slits resonance.

3. Near-Field Distributions

Next, we analyze the distributions of electric field amplitude and phase simultaneously to investigate the relation between transmission spectra and near-field features. The in-plane cut shown in Fig. 1(b) is along the silicon substrate side right after the back surface of thin metal film perforated with 2-D hole arrays, while the perpendicular-plane $\perp_x\ (\perp_y)$-plane cut is the x–z (y–z) plane cut along the center of $y\ (x)$-coordinate of the unit cell. According to Liu *et al.* [18], since the H-shaped hole pattern has twofold mirror symmetry, the components of electric field (E_x, E_y, and E_z) under normal incidence could be classified into four symmetric categories, which is summarized in Table 1. An incident field will preserve its particular symmetry when transmitting through subwavelength hole structures drilled in metallic film. Therefore, for *x*-polarized light, E_x has even–even symmetry, and E_y has odd–odd symmetry. On the other hand, for *y*-polarized light, E_x has odd–odd symmetry and E_y has even–even symmetry. For example, Fig. 4(a) shows ψ_x and ψ_y, respectively, at in-plane cut for ($\pm$2, 0) mode

TABLE 1

Categories of symmetry of electric field components for H-shaped holes. For samples 1 and 2, they only preserve the symmetry with respect to the center of the *y*-coordinate of the unit cell

Polarization state of the incident field	Field component	Symmetric category with respect to the center of the x-coordinate/y-coordinate
E_{xinc}	E_x	even/even
	E_y	odd/odd
	E_z	odd/even
E_{yinc}	E_x	odd/odd
	E_y	even/even
	E_z	even/odd

Ag/Si WA under *x*-polarized light and Fig. 4(b) shows those for (0, $\pm$2) mode Ag/Si WA under *y*-polarized light. These figures demonstrate that E_x and E_y indeed possess specific symmetries for H-shaped hole arrays. However, for samples 1 and 2, mirror symmetry with respect to the center of the *x*-coordinate no longer exists [see Fig. 4(c)–(d)].

3.1. *x*-Polarized Light

First, we analyze the near-field distributions corresponding to different orders of WA modes for samples 1 to 3 under *x*-polarized light, and we find that they all exhibit some similar features. For example, Fig. 5(a) shows the modulus of the electric field $|\mathbf{E}|$ at in-plane cut and the modulus of the electric field amplitude and the phase along the propagation direction, $|E_z|$ and ψ_z, at $\perp_x$-plane cut for $(\pm 1, \pm 1)$ Ag/Si WA modes at 35 μm, and Fig. 5(b) shows those for the adjacent surface EM modes at 34 μm of sample 3. Both $|\mathbf{E}|$ and $|E_z|$ display distinct field patterns at the Ag/Si interface for WAs and surface EM modes. By comparing the ψ_z distributions in Fig. 5(a) and (b), we find that ψ_z is quite homogeneous for WAs, while ψ_z has changed severely near the hole in the substrate for surface EM modes. According to Abajo *et al.* [23], the transmittance of the metallic hole array could be derived from the reflectance of the complementary metallic disk array by Babinet's principle. Therefore, the transmission for the metallic hole array can be expressed as

$$T = \frac{1}{1 + \left(\frac{A}{2\pi \times k} \mathrm{Re}\left[\frac{1}{\alpha_E} - G_E\right]\right)^2} \tag{2}$$

where A is the area of the unit cell, k is the light momentum in free space, α_E is the electric polarizability of the disks, and $G_E = \sum_{R \neq 0} (k^2 + \partial_{xx}^2) e^{ikR}/R$ is the summation of the dipole-dipole interaction dyadic under normal incidence. G_E diverges when one of the diffracted orders becomes grazing, which is the same condition that produces WAs and results in transmission minimum according to (2). The divergence of G_E is related to the accumulation of in-phase long-distance multiple scattering. This may be associated with the homogeneity of ψ_z for WAs in our near-field analyses. On the other hand, two channels are responsible for the EOT phenomenon as described by Fano [25]: One is simply the direct scattering of the field through the apertures and can be represented by a continuum of states, and the other is via a discrete resonant state (surface EM mode) and then coupled to the continuum of states. Besides, it is near those divergences associated with WAs that surface EM modes can exist [26]. Surface EM modes are confined to the surface and partially coupled to a continuum near the apertures, and thus resulting in the transmission peaks and the severe change of ψ_z. For samples 1 and 2, the ψ_z distributions are a little bit disordered due to the broken symmetry with respect to the center of the *x*-coordinate, but the distinct features of ψ_z for WAs and surface EM modes still reserve, as shown in Fig. 6.

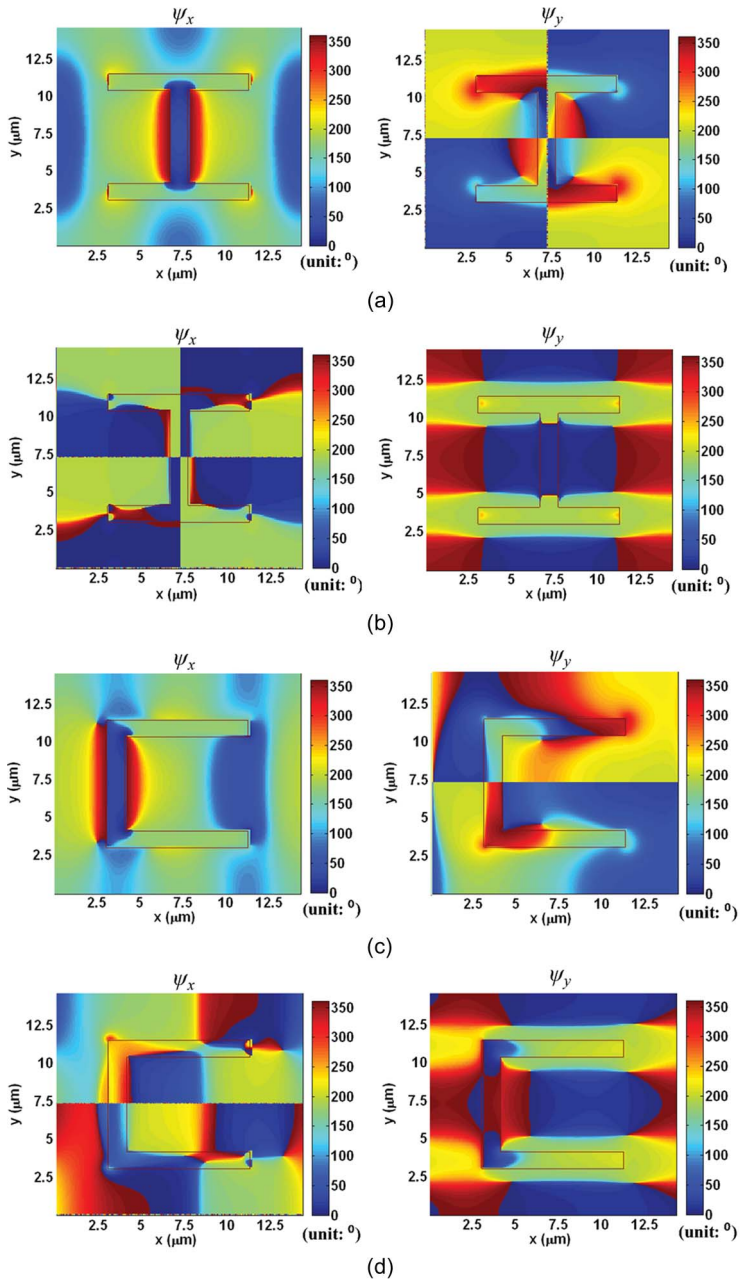

Fig. 4. For sample 3 within twofold mirror symmetry, E_x possesses even–even symmetry, and E_y possesses odd–odd symmetry under *x*-polarized light excitation, while E_x possesses odd–odd symmetry, and E_y possesses even–even symmetry under *y*-polarized light. For samples 1 and 2, mirror symmetry with respect to the center of the *x*-coordinate no longer exists. For example, the ψ_x and ψ_y distributions for ($\pm$2, 0) and (0, $\pm$2) Ag/Si WA are shown in (a) and (b) for sample 3 and in (c) and (d) for sample 1, respectively.

Next, we focus on the brand-band peaks in the spectra of Fig. 3(a) corresponding to the first U-shaped resonances for samples 1 to 3. As shown in Fig. 7, the large magnitude of |**E**| and the homogeneous distribution of ψ_x under *x*-polarized light within the shape resonant paths may result in the strong transmission. |**E**| also contours clear geometrical patterns of the resonant modes and $|E_z|$ at $\perp_y$-plane cut is strongly localized near the edge of the slits for SRs. $|E_z|$ for samples 2 and 3 are not shown since they demonstrate similar features. The most interesting part is that ψ_z exhibits a

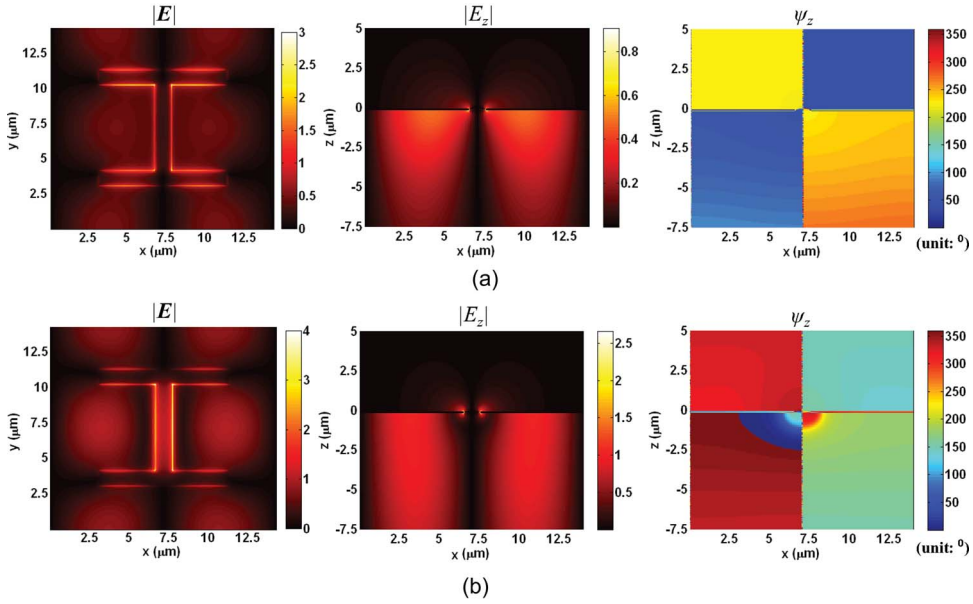

Fig. 5. |**E**| distribution at in-plane cut and $|E_z|$ and ψ_z distributions at $\perp_x$-plane cut of sample 3 at (a) 35 μm for $(\pm 1, \pm 1)$ WA and (b) 34 μm for the adjacent surface EM mode.

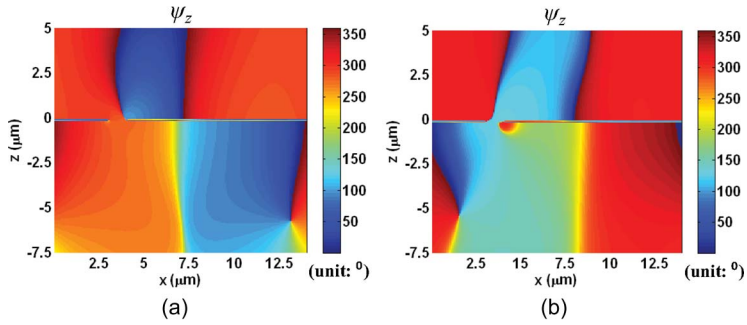

Fig. 6. ψ_z distributions at $\perp_x$-plane cut of sample 1 at (a) 35 μm for $(\pm 1, \pm 1)$ WA and (b) 34 μm for the adjacent surface EM mode. (Those for sample 2 demonstrate similar features.)

180° phase difference with respect to the center of the slit width along the shape resonant path. Therefore, the effective resonant lengths for SRs could be clearly determined by analyzing both |**E**| and ψ_z. For example, by analyzing the ψ_z distribution of sample 2, which could be divided into two possible U-shaped paths as shown in Fig. 1(a), we can clearly distinguish that the dominant resonant pattern at 96 μm is along the green path since ψ_z only processes 180° phase difference within that path. Moreover, for sample 3, ψ_z fulfills the requirement in two symmetric U-shaped holes as shown in Fig. 7(c), and thus, both paths would contribute to the resonance. Furthermore, since both measured and simulation transmission spectra exhibit peaks at 51 μm for sample 1 and at 52 μm for sample 2, we thus analyze the near-field features and find that the peak at 51 μm is related to the first *y*-arm slit SR, while that of sample 2 corresponds to the red-path [referring to Fig. 1(a)] U-shaped resonance. As shown in Fig. 8, |**E**| displays both features for surface EM modes and SRs: distinct field patterns at the Ag/Si interface indicating the characteristic of surface EM modes as well as contouring clear geometric patterns at the boundary of the hole for SRs. Besides, ψ_x and ψ_z exhibit the properties of homogeneity and the 180° phase difference within the shape resonant path, respectively, showing good agreement with the mentioned features for SRs.

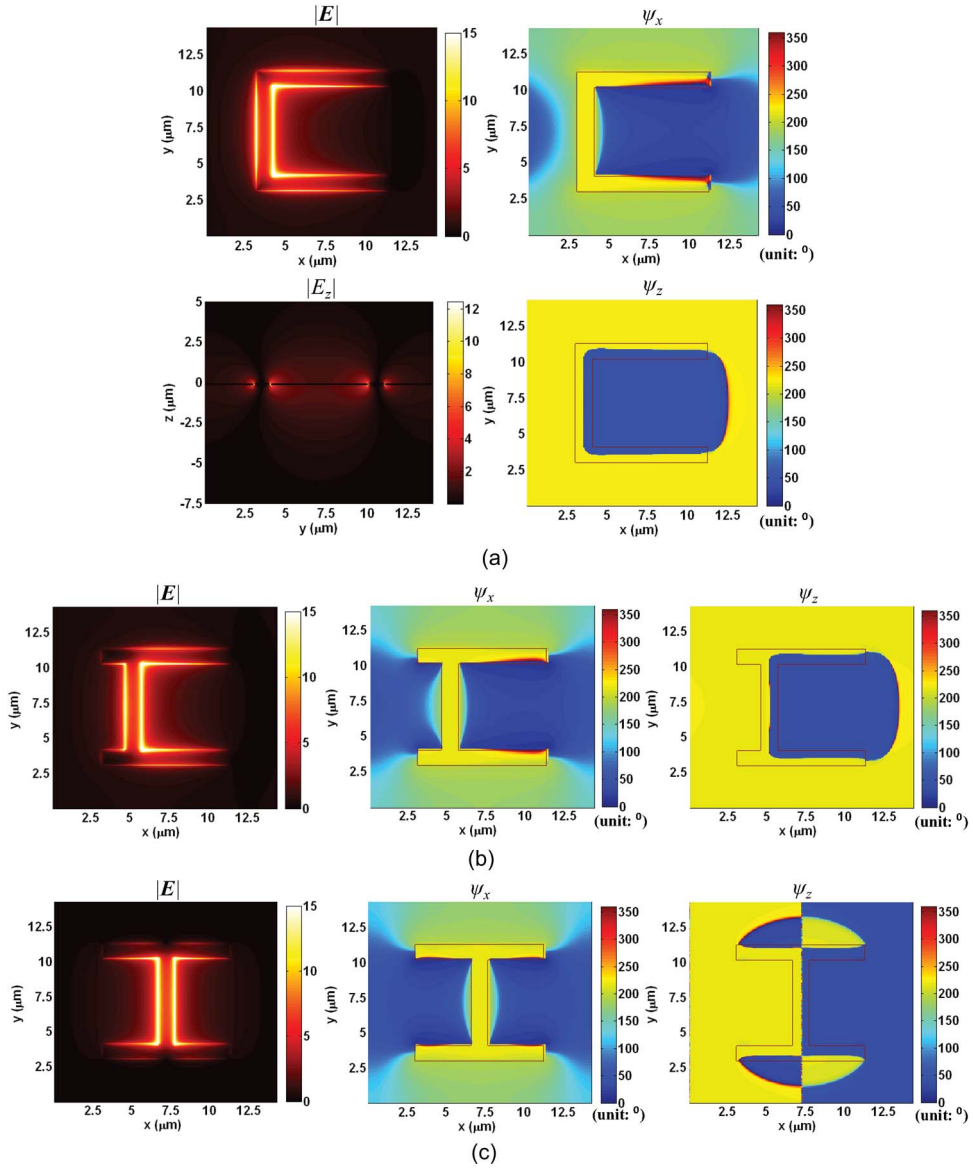

Fig. 7. $|\mathbf{E}|$, ψ_x, and ψ_z distributions at in-plane cut and $|E_z|$ distribution at $\perp_y$-plane cut corresponding to the first LSR for (a) sample 1 at 109 μm, (b) sample 2 at 96 μm, and (c) sample 3 at 87 μm.

3.2. *y*-Polarized Light

Fig. 9 shows the $|\mathbf{E}|$ distribution at in-plane cut and $|E_z|$ and ψ_z distributions at $\perp_y$-plane cut for $(\pm 1, \pm 1)$ Ag/Si WA modes at 35 μm and those for the adjacent surface EM modes at 34 μm of sample 1 under *y*-polarized light. Sample 2 demonstrates similar near-field features (not shown). Both $|\mathbf{E}|$ and $|E_z|$ display distinct field patterns at the Ag/Si interface for WAs and surface EM modes as in the case under *x*-polarized light. We again find the homogeneity of ψ_z for WAs and the severer phase change for surface EM modes, thus showing the consistency of the observation. Moreover, in order to check whether these features are general to WAs and adjacent surface EM modes, we have varied the structural parameters to examine their near-field distributions in the optical range. The same profiles have been observed, thus providing evidence that the different ψ_z distributions near the apertures are meaningful to the mentioned physical characteristics of WAs and adjacent surface EM modes.

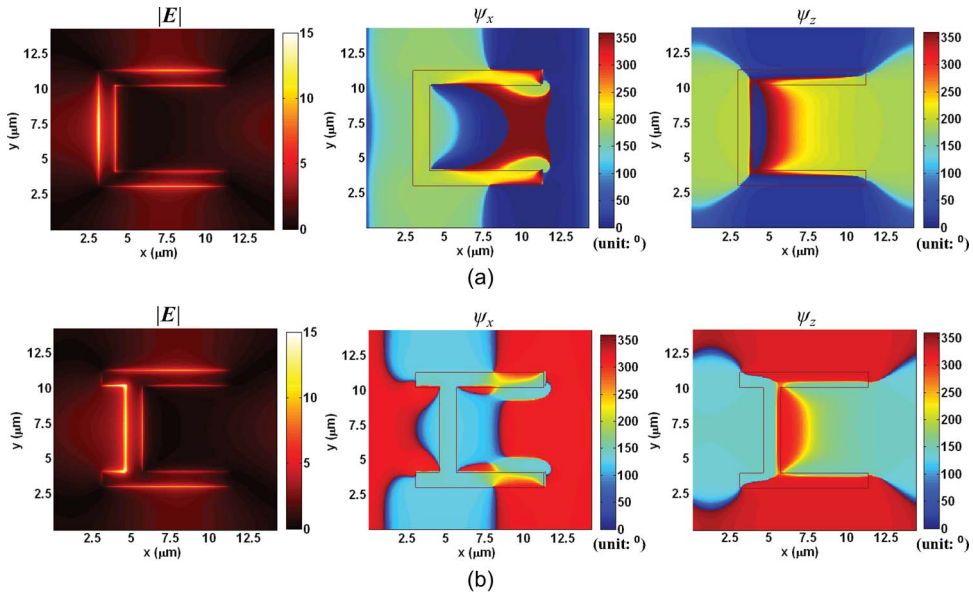

Fig. 8. $|\mathbf{E}|$, ψ_x, and ψ_z distributions at in-plane cut for (a) sample 1 at 51 μm and (b) sample 2 at 52 μm.

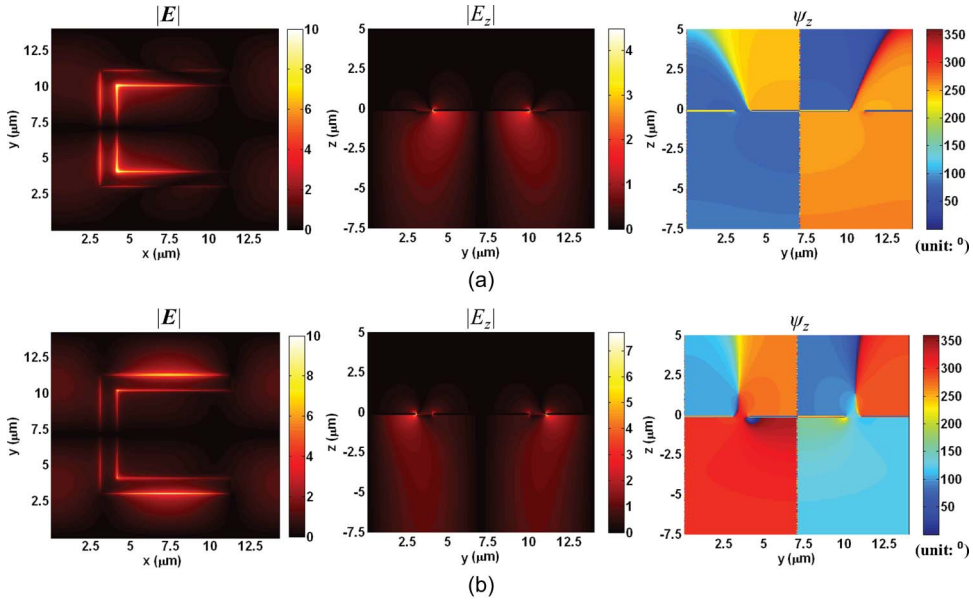

Fig. 9. $|\mathbf{E}|$ distribution at in-plane cut and $|E_z|$ and ψ_z distributions at $\perp_y$-plane cut of sample 1 at (a) 35 μm for $(\pm 1, \pm 1)$ WA and (b) 34 μm for the adjacent surface EM mode.

Finally, we focus on the broadband peaks in the spectra of Fig. 3(b). As shown in Fig. 10(a) and (b), the $|\mathbf{E}|$ distributions, which are concentrated near the boundaries of the hole with a node in the middle of the *y*-arm slit, demonstrate geometric resonant patterns of 2nd U-shaped resonances and ψ_y is quite homogenous under *y*-polarized light. Moreover, the $|E_z|$ distributions at $\perp_y$-plane cut are strongly localized near the edges of the slits and the ψ_z distributions exhibit a 180° phase difference with respect to the center of the slit width within the shape resonant paths, which all show determinative features for SRs. Notice that in Fig. 10(c), the ψ_z distribution owns the 180° phase difference with respect to the center of two *x*-arm slits' width only. The lack of phase difference in *y*-arm slit is due

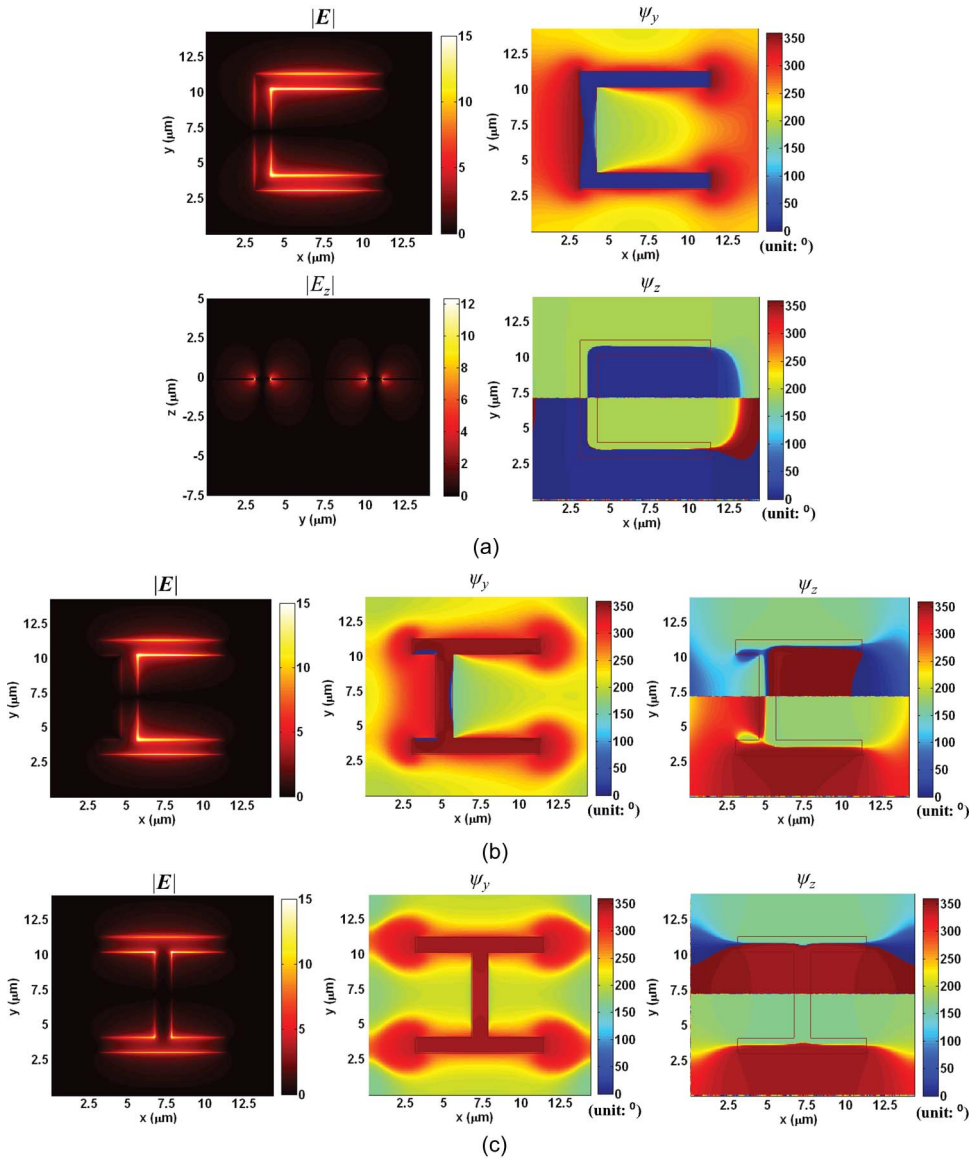

Fig. 10. $|\mathbf{E}|$, ψ_y, and ψ_z distributions at in-plane cut and $|E_z|$ distribution at $\perp_y$-plane cut corresponding to the second U-shaped resonances for (a) sample 1 at 51 μm, (b) sample 2 at 47 μm, and the two *x*-arm slits resonance for (c) sample 3 at 42 μm.

to the requirement of even symmetry with respect to the center of the *x*-coordinate for H-shaped holes under *y*-polarized light (see Table 1). For samples 1 and 2, there is no such symmetry requirement for their *y*-arm slits since the mirror symmetry with respect to the center of *x*-coordinate no longer exists. Besides, the SR has the priority to follow the longest possible path, thus exciting the second U-shaped resonance for samples 1 and 2, as well as the two *x*-arm slits resonance for sample 3. In order to validate that this resonance is associated with the two *x*-arm slits resonance rather than the second U-shaped resonance for sample 3, we enlarge the difference of effective resonant lengths between these two resonances by changing the separation distances l_y between the two *x*-arm slits from 8 μm to 6 μm and 4 μm, respectively. The effective lengths of the 2nd U-shaped resonance shrink from 15 μm to 13 μm and 11 μm, respectively, while those of the two *x*-arm slits resonance will not be affected by different l_y's and keeps at 8 μm. However, due to the great effects of WAs in shaping the spectral profiles [10], we could hardly tell the response of resonant wavelengths corresponding

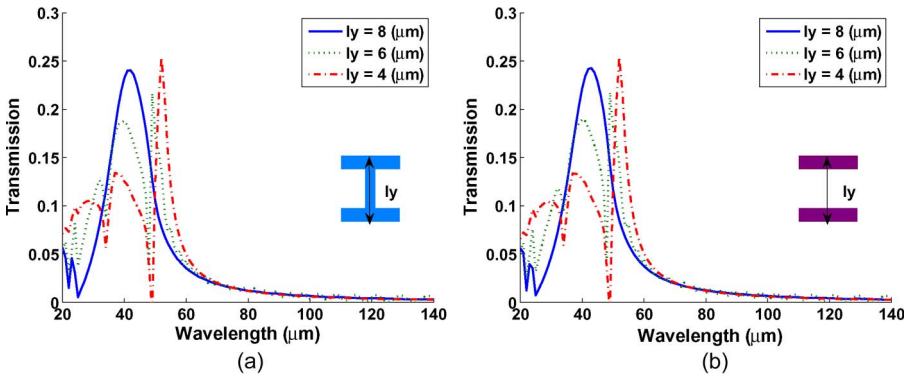

Fig. 11. Simulated transmission spectra for (a) H-shaped apertures and (b) two *x*-arm slits apertures under different separation distance l_y between the two *x*-arm slits.

to different separation distances. We thus simulate the same condition for merely the two *x*-arm slits aperture, as shown in Fig. 11, and find that the spectral profiles can almost overlap with each other under the same separation distance for the H-shaped and two *x*-arm slits apertures, therefore giving evidence to the fact that the peak at 42 μm is associated with the two *x*-arm slits resonance.

4. Conclusion

We find that by analyzing the distributions of the electric field amplitude and phase simultaneously, the unique near-field features associated with specific resonant modes can be summarized as follows. 1) For SRs, the large magnitude of $|\mathbf{E}|$ and the homogeneity of the phase component parallel to the polarization of the incident light within the shape resonant paths may result in transmission peaks. In order to determine the effective resonant lengths of SRs, we could use the properties of $|\mathbf{E}|$ and ψ_z: $|\mathbf{E}|$ contours a clear geometry pattern of the resonant mode, and ψ_z exhibits a 180° phase difference with respect to the center of the slit width along the shape resonant path. 2) $|E_z|$ is strongly localized near the edges of the slits for SRs, while $|E_z|$ display distinct field patterns at the Ag/Si interface for WAs or surface EM modes. 3) For WAs, ψ_z is quite homogeneous due to the accumulation of the in-phase multiple scattering; the weak coupling of surface EM modes to a continuum cause the transmission peaks and severe phase variation near the hole in the substrate.

We thus use such information to investigate the SR at the wavelength of 42 μm under *y*-polarized light because ψ_z exhibits 180° phase difference within the two *x*-arm slits only due to the requirement of even symmetry with respect to the center of the *x*-coordinate for H-shaped holes. The overlapped spectral profiles under the same separation distances between H-shaped and two *x*-arm slits apertures give us a clue that this resonance would be attributed to the two *x*-arm slits resonance.

References

[1] T. W. Ebbesen, H. J. Lezec, H. F. Ghaemi, T. Thio, and P. A. Wolff, "Extraordinary optical transmission through sub-wavelength hole arrays," *Nature*, vol. 391, no. 6668, pp. 667–669, Feb. 1998.
[2] H. F. Ghaemi, T. Thio, D. E. Grupp, T. W. Ebbesen, and H. J. Lezec, "Surface plasmons enhance optical transmission through subwavelength hole," *Phys. Rev. B*, vol. 58, no. 11, pp. 6779–6782, Sep. 1998.
[3] M. Sarrazin, J.-P. Vigneron, and J.-M. Vigoureux, "Role of Wood anomalies in optical properties of thin metallic films with a bidimensional array of subwavelength holes," *Phys. Rev. B*, vol. 67, no. 8, pp. 085415-1–085415-8, Feb. 2003.
[4] K. J. Klein Koerkamp, S. Enoch, F. B. Segerink, N. F. van Hulst, and L. Kuipers, "Strong influence of hole shape on extraordinary transmission through periodic arrays of subwavelength holes," *Phys. Rev. Lett.*, vol. 92, no. 18, pp. 183901-1–183901-4, May 2004.
[5] Z. Ruan and M. Qiu, "Enhanced transmission through periodic arrays of subwavelength holes: The role of localized waveguide resonances," *Phys. Rev. Lett.*, vol. 96, no. 23, pp. 233901-1–233901-4, Jun. 2006.

[6] J. W. Lee, M. A. Seo, D. H. Kang, K. S. Khim, S. C. Jeoung, and D. S. Kim, "Terahertz electromagnetic wave transmission through random arrays of single rectangular holes and slits in thin metallic sheets," *Phys. Rev. Lett.*, vol. 99, no. 13, pp. 137401-1–137401-4, Sep. 2007.
[7] K. L. van der Molen, K. J. Klein Koerkamp, S. Enoch, F. B. Segerink, N. F. van Hulst, and L. Kuipers, "Role of shape and localized resonances in extraordinary transmission through periodic arrays of subwavelength holes: Experiment and theory," *Phys. Rev. B*, vol. 72, no. 4, p. 045421, 2005.
[8] F. J. García-Vidal, E. Moreno, J. A. Porto, and L. Martín-Moreno, "Transmission of light through a single rectangular hole," *Phys. Rev. Lett.*, vol. 95, no. 10, pp. 103901-1–103901-4, Sep. 2005.
[9] A. Mary, S. G. Rodrigo, L. Martín-Moreno, and F. J. García-Vidal, "Theory of light transmission through an array of rectangular holes," *Phys. Rev. B*, vol. 76, no. 19, pp. 195414-1–195414-5, Nov. 2007.
[10] Y.-W. Jiang, L. D. Tzuang, Y.-H. Ye, Y.-T. Wu, M.-W. Tsai, C.-Y. Chen, and S.-C. Lee, "Effect of Wood's anomalies on the profile of extraordinary transmission spectra through metal periodic arrays of rectangular subwavelength holes with different aspect ratio," *Opt. Exp.*, vol. 17, no. 4, pp. 2631–2637, Feb. 2009.
[11] A. Degiron and T. W. Ebbesen, "The role of localized surface plasmon modes in the enhanced transmission of periodic subwavelength apertures," *J. Opt. A, Pure Appl. Opt.*, vol. 7, no. 2, p. S90, Jan. 2005.
[12] E. X. Jin and X. Xu, "Finite-difference time-domain studies on optical transmission through planar nano-apertures in a Metal Film," *Jpn. J. Appl. Phys.*, vol. 43, no. 1, pp. 407–417, Jan. 2004.
[13] H. Guo, T. P. Meyrath, T. Zentgraf, N. Liu, L. Fu, H. Schweizer, and H. Giessen, "Optical resonances of bowtie slot antennas and their geometry and material dependence," *Opt. Exp.*, vol. 16, no. 11, pp. 7756–7766, May 2008.
[14] F. Eftekhari and R. Gordon, "Enhanced second harmonic generation from noncentrosymmetric nanohole arrays in a gold Film," *IEEE J. Sel. Topics Quantum Electron.*, vol. 14, no. 6, pp. 1552–1558, Nov./Dec. 2008.
[15] J. W. Lee, M. A. Seo, D. J. Park, D. S. Kim, S. C. Jeoung, C. Lienau, Q.-H. Park, and P. C. M. Planken, "Shape resonance omni-directional terahertz filters with near-unity transmittance," *Opt. Exp.*, vol. 14, no. 3, pp. 1253–1259, Feb. 2006.
[16] M. Turkmen, S. Aksu, A. E. Cetin, A. A. Yanik, A. Artar, and H. Altug, "U-Shaped nano-apertures for enhanced optical transmission and resolution," in *Proc. SPIE*, 2011, vol. 8034, pp. 80340H-1–80340H-6.
[17] M. Sun, R. J. Liu, Z. Y. Li, B. Y. Cheng, D. Z. Zhang, H. F. Yang, and A. Z. Jin, "Enhanced near-infrared transmission through periodic H-shaped arrays," *Phys. Lett. A*, vol. 365, no. 5/6, pp. 510–513, Jun. 2007.
[18] R.-J. Liu, J.-X. Fu, and Z.-Y. Li, "Near-field analysis of the transmission properties of subwavelength periodic H-shaped arrays in thin metal film," *J. Opt.*, vol. 12, no. 6, p. 065002, May 2010.
[19] H.-F. Huang, Y.-W. Jiang, H.-H. Chen, Y.-T. Wu, Y.-T. Chang, F.-T. Chuang, and S.-C. Lee, "Localized shape resonance on silver film perforated by H-shaped and more complex shaped hole arrays," *Opt. Exp.*, vol. 19, no. 6, pp. 5225–5231, Mar. 2011.
[20] A. Taflove, *Computational Electrodynamics: The Finite-Difference Time-Domain Method,* 3rd ed. Norwood, MA: Artech House, 2005.
[21] M. Schnell, A. García-Etxarri, A. J. Huber, K. Crozier, J. Aizpurua, and R. Hillenbrand, "Controlling the near-field oscillations of loaded plasmonic nanoantennas," *Nat. Photon.*, vol. 3, no. 5, pp. 287–291, May 2009.
[22] M. Schnell, A. García-Etxarri, A. J. Huber, K. B. Crozier, A. Brisov, J. Aizpurua, and R. Hillenbrand, "Amplitude- and phase-resolved near-field napping of infrared antenna modes by transmission-mode scattering-type near-field microscopy," *J. Phys. Chem. C*, vol. 114, no. 16, pp. 7341–7345, 2010.
[23] F. J. García de Abajo, R. Gómez-Medina, and J. J. Sáenz, "Full transmission through perfect-conductor subwavelength hole arrays," *Phys. Rev. E*, vol. 72, no. 1, pp. 016608-1–016608-4, Jul. 2005.
[24] F. J. García-Vidal, L. Martín-Moreno, T. W. Ebbesen, and L. Kuipers, "Light passing through subwavelength apertures," *Rev. Mod. Phys.*, vol. 82, no. 1, pp. 729–787, Jan./Mar. 2010.
[25] U. Fano, "Effects of configuration interaction on intensities and phase shifts," *Phys. Rev.*, vol. 124, no. 6, pp. 1866–1878, Dec. 1961.
[26] F. J. García de Abajo and J. J. Sáenz, "Electromagnetic surface modes in structured perfect-conductor surfaces," *Phys. Rev. Lett.*, vol. 95, no. 23, pp. 233901-1–233901-4, Dec. 2005.
[27] E. D. Palik, *Handbook of Optical Constants of Solids.* London, U.K.: Academic, 1985.
[28] J. B. Pendry, L. Martin-Moreno, and F. J. García-Vidal, "Mimicking surface plasmons with structured surfaces," *Science*, vol. 305, no. 5685, pp. 847–848, Aug. 2004.